

1

## 2 Gentle rhodamines for live-cell fluorescence microscopy

3

4 Tianyan Liu<sup>1,2,10</sup>, Julian Kompa<sup>3,10</sup>, Jing Ling<sup>1,2,10</sup>, Nicolas Lardon<sup>3</sup>, Yuan Zhang<sup>1</sup>, Jingting Chen<sup>1</sup>, Luc Reymond<sup>4</sup>, Peng Chen<sup>5,6</sup>,  
5 Mai Tran<sup>3</sup>, Zhongtian Yang<sup>1,2</sup>, Haolin Zhang<sup>1,2</sup>, Yitong Liu<sup>1,2</sup>, Stefan Pitsch<sup>7</sup>, Peng Zou<sup>2,8</sup> Lu Wang<sup>9</sup>, Kai Johnsson<sup>3,4</sup>, Zhixing  
6 Chen<sup>1,2,5,6\*</sup>

7

8 1. College of Future Technology, Institute of Molecular Medicine, National Biomedical Imaging Center, Beijing Key  
9 Laboratory of Cardiometabolic Molecular Medicine, Peking University, Beijing 100871, China

10 2. Peking-Tsinghua Center for Life Science, Academy for Advanced Interdisciplinary Studies, Peking University, Beijing  
11 100871, China

12 3. Department of Chemical Biology, Max Planck Institute for Medical Research, Heidelberg 69120, Germany;

13 4. Biomolecular Screening Facility, École Polytechnique Fédérale de Lausanne (EPFL), Lausanne 1015, Switzerland

14 5. PKU-Nanjing Institute of Translational Medicine, Nanjing 211800, China

15 6. GenVivo Tech, Nanjing 211800, China

16 7. Spirochrome AG, Chalberwiedstrasse 4, CH-8260 Stein am Rhein, Switzerland.

17 8. College of Chemistry and Molecular Engineering, Synthetic and Functional Biomolecules Center, Beijing National  
18 Laboratory for Molecular Sciences, Key Laboratory of Bioorganic Chemistry and Molecular Engineering of the Ministry of  
19 Education, PKU-IDG/McGovern Institute for Brain Research, Peking University, Beijing 100871, China

20 9. Key Laboratory of Smart Drug Delivery, Ministry of Education, School of Pharmacy, Fudan University, 201203  
21 Shanghai, China;

22 10. Equal contribution

23

24 \*Corresponding author: Zhixing Chen (zhixingchen@pku.edu.cn)

25

## 26 Abstract

27 Rhodamines have been continuously optimized in brightness, biocompatibility, and colors to fulfill the  
28 demands of modern bioimaging. However, the problem of phototoxicity caused by the excited fluorophore  
29 under long-term illumination has been largely neglected, hampering their use in time-lapse imaging. Here we  
30 introduce cyclooctatetraene (COT) conjugated rhodamines that span the visible spectrum and exhibit  
31 significantly reduced phototoxicity. We identified a general strategy for the generation of Gentle Rhodamines,  
32 which preserved their outstanding spectroscopic properties and cell permeability while showing an efficient  
33 reduction of singlet-oxygen formation and diminished cellular photodamage. Paradoxically, their  
34 photobleaching kinetics do not go hand in hand with reduced phototoxicity. By combining COT-conjugated  
35 spirocyclization motifs with targeting moieties, these gentle rhodamines compose a toolkit for time-lapse  
36 imaging of mitochondria, DNA, and actin and synergize with covalent and exchangeable HaloTag labeling of  
37 cellular proteins with less photodamage than their commonly used precursors. Taken together, the Gentle  
38 Rhodamines generally offer alleviated phototoxicity and allow advanced video recording applications,  
39 including voltage imaging.

## 40 Introduction

41 Modern fluorescence microscopy has evolved from 3D imaging of fixed specimens to 4D-recording of  
42 subcellular structures or dynamic cellular processes in live cells or animals. Herein, a spatial resolution beyond  
43 the diffraction barrier and a temporal resolution of video rates can be achieved<sup>1-3</sup>. However, time-lapse  
44 recording at high resolution subjects the live samples to significantly elevated light doses, surpassing orders of  
45 magnitude the levels employed in typical one-shot wide-field or confocal imaging experiments.<sup>4</sup> High  
46 excitation light exposure of fluorescent labels is known to compromise the physiological integrity of biological  
47 samples<sup>5-7</sup>. This phenomenon, referred to as phototoxicity, is the reversible or irreversible damaging effect of  
48 light and fluorophores on living cells or organisms. Phototoxicity mainly originates from reactive oxygen  
49 species (ROS), which are generated by the excited states of chromophores<sup>6-8</sup>. A major ROS relevant to  
50 phototoxicity in live-cell fluorescence microscopy is singlet oxygen, which is the product derived from the  
51 reaction of the excited fluorophore and molecular oxygen<sup>9-11</sup>. The reactive singlet oxygen can oxidize nearby  
52 biomacromolecules such as lipids, carbohydrates, and nucleic acids, thereby affecting their physiological  
53 functions<sup>11-15</sup>. Such harmful effects accumulate over time and result in abnormal cell metabolism, deformation  
54 of organelles and organisms, arrested cell proliferation, and apoptosis<sup>7,16-18</sup>. Therefore, phototoxicity is a  
55 universal phenomenon that widely affects live-cell fluorescence imaging practice, rendering it potentially  
56 invasive. With the democratization of super-resolution imaging and time-lapse imaging instruments,  
57 minimizing phototoxicity is of growing importance to endorse the physiological relevance of the recorded data  
58 in bioimaging.

59  
60 From the perspective of photophysical chemistry, phototoxicity, and photobleaching are generally believed to  
61 stem from the excited triplet states (Fig. 1a). Triplet state quenchers (TSQs), such as mercaptoethylamine  
62 (MEA) or cyclooctatetraene (COT), have a rich history of serving as protective agents in live-cell fluorescence  
63 imaging<sup>11,19-23</sup>. In the past decade, the direct conjugation of such TSQ moiety on a selected dye scaffold has  
64 been proposed as a strategy for increasing photostability<sup>19,20</sup>, particularly demonstrated with single-molecule  
65 imaging using cyanine dyes. Recently, our laboratory and others repurposed these photophysically  
66 sophisticated molecules for live-cell super-resolution imaging of mitochondria and voltage imaging<sup>11,21-23</sup>,  
67 where phototoxicity has emerged as a complementary threat to photobleaching. These pioneering works are  
68 niche demonstrations tailored for a small number of cellular structures using cyanine or fluorescein dyes, whose  
69 charged chemical nature limits their general biological applications.

70  
71 Rhodamine dyes featuring excellent photophysical properties, spectral tunability, and cell permeability, have  
72 dominated the field of live-cell fluorescent imaging in recent years. Particularly, silicone rhodamine-(SiR)<sup>24</sup>-  
73 carboxyl-based probes (SiR-actin<sup>25</sup>, SiR-tubulin<sup>25</sup>, and SiR-Hoechst<sup>26</sup>) possessing fluorogenicity<sup>24,27</sup> due to an  
74 environmentally-sensitive equilibrium between a fluorescent zwitterion and a non-fluorescent spirolactone,  
75 helped to increase the cell-permeability and reduce the background fluorescence in live-cell imaging. In  
76 addition, a general strategy tuning this dynamic equilibrium by introducing (sulfon)amide modifications to the  
77 3-carboxylic acid was subsequently established to create multi-color fluorogenic rhodamines for live-cell  
78 nanoscopy<sup>28</sup>. To meet the growing demands of fluorescence nanoscopy, the photophysical properties of dyes  
79 such as brightness<sup>29,30</sup>, photostability<sup>31-34</sup>, and blinking<sup>35,36</sup> have been further engineered. Most importantly,  
80 rhodamine can be used in conjunction with a variety of labeling techniques for instance self-labeling protein  
81 tags (HaloTag<sup>37</sup>, SNAP-tag<sup>38,39</sup>, and TMP-tag<sup>40</sup>), tetrazine for click chemistry<sup>41</sup>, biomolecular ligands<sup>25</sup> and  
82 specific ligands for organelles<sup>25,26</sup>. This synergistic development has also consolidated rhodamine as a  
83 mainstream tool for bioimaging. From the phototoxicity perspective, the systematic upgrading of rhodamines

84 towards reduced ROS generation would lead to another breakthrough for imaging tools in the field of 4D  
85 fluorescence imaging<sup>18</sup>.

86  
87 Here, we introduced a general TSQ-conjugation strategy to reduce the phototoxicity of rhodamine derivatives.  
88 As confirmed by *in vitro* singlet-oxygen production or protein damage assays, as well as live-cell phototoxicity  
89 studies to various sub-cellular compartments, Gentle Rhodamines (GR) are valuable tools for light-intense  
90 microscopy applications. Interestingly, the TSQ-rhodamine derivatives do not necessarily bear enhanced  
91 photostability, implying alternative photobleaching pathways that are independent of triplet state populations.<sup>42</sup>  
92 This strategy is compatible with a broad range of fluorogenic rhodamine derivatives and popular live-cell  
93 labeling strategies such as self-labeling tags or ligands for subcellular structures, bringing out a practical dye  
94 palette for general and gentle imaging of mitochondria, plasma membrane, nucleus, cytoskeleton, and proteins  
95 of interest in mammalian cells. We demonstrate, that GR probes can be combined with microscopy techniques  
96 like time-resolved STED and functional imaging of the membrane potential in cardiomyocytes.  
97

## 98 Results

### 99 Generation of gentle tetramethyl rhodamine through COT conjugation at the 3-carboxyl position

100  
101 To systematically profile the structure-activity relationship of rhodamine-TSQ conjugates, we selected COT  
102 and nitrobenzene as representative TSQs and synthesized their rhodamine derivatives. Cyclooctatetraene-1-  
103 menthanol was conjugated to the lower pendant ring of tetramethyl rhodamine (TMR) via the 3-, 4-, or 5-  
104 carboxylic acid to yield compound **2-4** and nitrobenzene was coupled to 3-carboxy TMR as compound **5** (Fig.  
105 1b and Supplementary Fig. S1a-e, see Method for details). It has been previously demonstrated that TSQs  
106 affect the photophysics of Cy5 in a distance-dependent manner<sup>43</sup>. X-ray crystallography analysis of compound  
107 **2 (GR555M)** highlights the proximity between the xanthene chromophore and the COT moiety  
108 (Supplementary Fig. S2). Notably, the COT moiety is conformationally flexible as evident from the two  
109 components in the single crystal, further enhancing its effective collision with the chromophore.

110 Subsequently, the TSQ-TMR conjugates, along with the reference compound TMR methyl ester (**TMRM**,  
111 compound **1**), were evaluated from three aspects: (i) photostability; (ii) singlet oxygen generation *in vitro*; and  
112 (iii) phototoxicity based on a cell apoptosis assay. First, we measured the photobleaching curves of the five  
113 compounds. In organic polymer films (poly methyl methacrylate and vinyl alcohol), mimicking the amphiphilic  
114 environment present in cells, compounds **1-4** show high and comparable photostability. Instead, nitrobenzene  
115 compound **5** was significantly more susceptible to photobleaching (Fig. 1c and Supplementary Fig. S1f). In  
116 aqueous PBS buffer, the COT derivatives are the least photostable likely due to poor hydrophilicity  
117 (Supplementary Fig. S3). Overall, the TSQ-conjugated tetramethyl rhodamines give unpredictable trends on  
118 photostability. Next, all TSQ-conjugated dyes exhibited reduced singlet oxygen generation (Fig. 1d, e and Table  
119 S1), as measured by the singlet oxygen-induced decay of 1,3-diphenylisobenzofuran (DPBF) under the  
120 illumination of a green LED lamp (50 mW/cm<sup>2</sup>, 520-530 nm).<sup>44</sup> The lowest singlet oxygen quantum yield was  
121 measured with the TMR derivative bearing COT in the closest proximity (3-carboxy) to the chromophore  
122 (compound **2**,  $\Phi_{\Delta}: 2.1 \pm 0.1 \times 10^{-3}$ ), which is 6-fold reduced compared to that of **TMRM** (compound **1**,  $\Phi_{\Delta}: 2.2$   
123  $\pm 0.4 \times 10^{-2}$ , Fig. 1e and Table S1). Finally, we stained HeLa cells with compound **1-5** (250 nM) to assess the  
124 phototoxicity through a photo-induced apoptosis assay. The positive charge of these dyes leads to a bright  
125 fluorescent signal inside mitochondria, an organelle that is vulnerable to photodamage leading to apoptosis.  
126 Illumination of the cells for different time periods was performed in a high-content imager before assessing

127 apoptosis using propidium iodide (PI) stain. The half-lethal light dose for cells stained with compound **1** was  
128 reached after 2 min-illumination, while it required 2-5 min-illumination for the TSQ-conjugated compound **3-5**  
129 to kill 50% of the cells. Remarkably, for compound **2**, the dose was reached after 10 min-illumination,  
130 meaning that such a probe could extend the duration of time-lapse recording by about five times compared to  
131 **1** (Fig. 1f). These data corroborate our previous work on COT-conjugated cyanines<sup>11,22</sup>, confirming that the  
132 reducing effect of TSQs on phototoxicity can be largely independent on their effect on photostability. Also, we  
133 proved that COT is a privileged TSQ for reducing the phototoxicity of fluorophores across different scaffolds  
134 like cyanines and rhodamines. In summary, COT-conjugation at 3-carboxyl of TMR can achieve the largest  
135 reduction in phototoxicity among the screened isomers and leads to bright and specific staining of mitochondria,  
136 wherefore we named this probe **GR555M**.

137  
138 Having identified **GR555M** as a gentle rhodamine dye, we coupled it to wheat germ agglutinin (WGA) via its  
139 succinimidyl ester (**S25**, Supplementary Fig. S4a) yielding **GR555PM**. WGA is a lectin that binds to sialic  
140 acid and N-acetylglucosaminyl residues located on the extracellular surface of most mammalian cells<sup>45</sup> and  
141 presents an established strategy for labeling and imaging the plasma-membrane of live cells. **GR555PM** works  
142 as a bright fluorescent plasma-membrane marker on live HeLa cells (Fig. 1g, h). We monitored its cellular  
143 phototoxicity in comparison to **WGA-TMRM** in a high-content imager by assessing cell viability using  
144 Calcein AM stain after continuous imaging of the labeled membranes. Compared to **WGA-TMRM**, our COT-  
145 bearing variant **GR555PM** showed lower cellular phototoxicity by a factor of four with a half-lethal dose of  
146 10 min-illumination (Fig. 1i). This assay confirmed the reduced phototoxicity of COT-conjugated rhodamines,  
147 at the same time presenting a practical and gentle membrane stain.

148  
149

## 150 COT-conjugation gives gentle rhodamines with diverse auxochromes at various colors.

151

152 Next, we extended our design to other commonly used rhodamine derivatives with wavelengths that range  
153 from green to far red. Green-emitting Rhodamine 110 and far red-emitting SiR dyes were esterified with COT-  
154 alcohol, giving rise to two novel mitochondrial dyes, **7 (GR510M)** and **9 (GR650M)**, that offer reduced singlet  
155 oxygen generation than their methyl-ester counterparts, **6 (Rho123)** and **8 (SiRM)** (Fig. 2a-e and Table S1).  
156 Compound **7** and **9** differed in their bleaching behaviors relative to their parental compounds (**6** and **8**). These  
157 differences in photobleaching rate are environmentally dependent (Supplementary Fig. S5 and S6).  
158 Corroborating our studies on tetramethyl rhodamines, no general improvement of the bleaching resistance of  
159 COT-conjugated rhodamines with different colors was evident. Moreover, we esterified JF<sub>549</sub> bearing azetidine  
160 auxochromes and Rhodamine 101 bearing julolidine auxochromes with COT alcohol (Compound **11** and **13**,  
161 Fig. 2a and Supplementary Fig. S7). Both compounds exhibited drastically reduced singlet-oxygen generation  
162 (Figure 2d, e). Overall, COT-conjugation is a general approach to alleviate the phototoxicity of the state-of-  
163 the-art rhodamine palette.

164

165 We then performed the light-induced apoptosis assay with this set of gentle mitochondrial dyes. Unlike the  
166 TMR derivatives which trigger apoptosis under light-illumination, **Rho123** and **GR510M** rapidly escaped from  
167 mitochondria before the induction of apoptosis, most likely due to a higher hydrophilicity. We first verified  
168 that **GR510M** is a fast-acting mitochondrial membrane potential (MMP) indicator like **Rho123**, by recording  
169 of a rapid decrease in fluorescent intensity after the addition of the mitochondrial oxidative phosphorylation  
170 uncoupler, carbonyl cyanide 3-chlorophenylhydrazone (CCCP) (Fig. 2f and Supplementary Fig. S8), which  
171 means that the drop of **GR510M** or **Rho123** signal could indicate the MMP level and further reflect the  
172 mitochondrial health. Therefore, for **Rho123** and **GR510M**, phototoxicity was evaluated by their light-induced  
173 decrease in mitochondrial fluorescence. In continuous time-lapse recordings of stained live cells, the MMP of

174 the cells treated with **GR510M** decreased by 50% after 1 min-illumination with a blue LED (488 nm, 1.7  
175 W/cm<sup>2</sup>), whereas the control compound **Rho123** showed a more rapid decrease of MMP with a half-life of  
176 only 0.5 min (Supplementary Fig. S9). The *in-vitro* and *in-cellulo* assays collectively proved that COT-  
177 conjugation can reduce the phototoxicity of the green **R110** dye by a factor of two. Unlike the **Rho123**  
178 derivatives that dissipate from mitochondria instantaneously upon photodamage, the far-red rhodamine  
179 **GR650M** and **SiRM** exhibited a slower photo-induced leakage kinetics and induced cell death, likely due to  
180 their higher hydrophobicity. Therefore, the photo-induced apoptosis assay can be used to assess the cellular  
181 phototoxicity. The half-lethal light dose of the cells stained with **GR650M** was reached after 10-15 min-  
182 illumination with a red LED (650 nm, 1.2 W/cm<sup>2</sup>), which is 5-7-fold higher than that of **SiRM** (half-lethal at 2  
183 min illumination) (Fig. 2g). These results demonstrated that the COT-conjugation reduces singlet oxygen  
184 generation and cellular phototoxicity of rhodamine derivatives with different colors.

185

186 As practical mitochondrial stains, cyanine-COT conjugates generally give stronger fluorescence signals than  
187 rhodamines. Yet our selected rhodamine-mito series complements the **PK Mito** probes in the green to yellow  
188 spectral range (**GR510M**, **GR555M**) and, unlike the lipophilic cyanines, **GR510M** enables instantaneous  
189 response to inner membrane potential changes for time-lapse functional imaging of mitochondria. Moreover,  
190 **GR650M** like other SiR-based probes has far-red emission and a similar quantum yield compared to its parent  
191 compound **SiRM** (Table S2). We demonstrate the compatibility with commercial STED nanoscopy systems  
192 equipped with a 775-nm depletion laser by the visualization of the cristae organization of COS-7 cells, which  
193 enabled us to distinguish adjacent crista at the spacing of 66 nm (Fig. 2h, i). Overall, rhodamine-COT based  
194 mitochondrial dyes supplement and supplant their cyanine counterparts (such as **PK Mito** dyes<sup>11,22</sup>) for  
195 mitochondrial recordings.

196

197

## 198 **Fluorogenic COT-rhodamines exhibit lower phototoxicity for general organelle imaging**

199

200 The emerging class of fluorogenic rhodamines, bearing a dynamic equilibrium between a fluorescent zwitterion  
201 and a nonfluorescent spirolactone/lactam form, have enabled wash-free imaging of various organelles.<sup>28</sup> We  
202 speculated that the COT-conjugation of rhodamines can be integrated into the spirocyclization motif, in which  
203 a COT-sulfonamide group instead of a COT-methanol is introduced to the 3- position, giving a cell-permeable  
204 and fluorogenic rhodamine core.

205

206 We first derivatized the fluorogenic TMR-COT conjugate with Hoechst at the 5-carboxyl position, yielding  
207 **GR555-DNA (15)** (Fig. 3a). **GR555-DNA** exhibited an 8-fold fluorescent intensity increase (“turn-on”) upon  
208 binding to hairpin-DNA (hpDNA) *in vitro*, exhibiting a higher fluorogenicity than **MaP555-DNA** and a  
209 comparable fluorescence quantum yield (Supplementary table S3). Compared to the parent compound  
210 **MaP555-DNA (14)**, the COT-derived counterpart exhibited 8-fold lower singlet oxygen generation under LED  
211 illumination (520-530 nm, 50 mW/cm<sup>2</sup>, Fig. 3b and Table S1).

212

213 For live-cell staining, **GR555-DNA** showed nuclear specificity. The new DNA stain displayed a lower cell-  
214 permeability than **MaP555-DNA**, presumably due to a larger molecular weight. Yet for HeLa cells staining,  
215 labeling with 2  $\mu$ M **GR555-DNA** or 0.2  $\mu$ M **MaP555-DNA** for 60 min resulted in similar brightness and signal-  
216 to-noise ratios under no-wash conditions (Supplementary Fig. S10a). Notably, the staining conditions of  
217 **GR555-DNA**, although slightly more demanding, did not lead to significant cytotoxicity (Supplementary Fig.  
218 S11). We then exploited a DNA repair imaging assay to semi-quantitatively characterize the phototoxicity of  
219 DNA dyes in live cells (schematic diagram shown in Fig. 3c). X-ray cross-complementing protein 1 (XRCC1)  
220 is a scaffolding protein that accumulates at sites of DNA-damage and recruits other proteins involved in DNA

221 repair pathways.<sup>46</sup> hXRCC1-GFP is evenly distributed in the nucleus of healthy cells, while upon DNA damage  
222 it gets recruited to the damaged site and exhibits multiple fluorescent puncta patterns in the nucleus, giving a  
223 sensitive assay of DNA damage under stress.<sup>47</sup> HeLa cells expressing hXRCC1-GFP labeled with **MaP555-**  
224 **DNA** showed a gradual increase in the number of hXRCC1-GFP puncta after 2 min-exposure to a 560 nm  
225 pulse laser, and the puncta numbers plateaued after 10 min-exposure. In contrast, HeLa cells labeled with  
226 **GR555-DNA** had a lower number of hXRCC1-GFP puncta than those treated with **MaP555-DNA** (Fig. 3d, e).  
227 To control the photobleaching factors, we also compared the *in cellulo* photostability of the **GR555-DNA** and  
228 **MaP555-DNA**. Neither of the two DNA dyes showed significant fluorescence intensity decay after 12 min of  
229 exposure to the 560 nm pulsed laser (Supplementary Fig. S10b). Therefore, we concluded that the COT-  
230 conjugation strategy reduced the cellular phototoxicity when such fluorophore is attached to a DNA-targeting  
231 moiety and ultimately minimize the DNA damage in live-cell microscopy.

232

233 Next, we aimed to develop a low-phototoxicity probe for imaging of the cytoskeleton in live cells. We  
234 conjugated **GR555** to a Jasplakinolide derivative binding to F-actin<sup>25</sup> yielding **GR555-Actin** (compound 17,  
235 Fig. 3f). **GR555-Actin** has a ~6-fold reduced singlet oxygen generation compared to the reference dye  
236 **MaP555-Actin** (compound 16, Supplementary Fig. S12 and Table S1). In long-term time-lapse confocal  
237 imaging, **GR555-Actin** exhibited reduced phototoxicity and enhanced brightness and photostability  
238 (Supplementary Fig. S13). Actin filaments of HeLa cells stained with **MaP555-Actin** tend to shrink,  
239 accompanied by a large attenuation of the fluorescence intensity, and gradually disintegrated and fractured into  
240 short strands after 41-47 min (350-400 frames). In comparison, **GR555-Actin** enabled acquisitions of 118 min  
241 (1000 frames) with integral actin filament structures (Fig. 3g and Supplementary Movie S1). Together, these  
242 data demonstrate that the COT-conjugated actin probe enables long-term imaging of cellular structures with  
243 low phototoxicity.

244

245

## 246 Fluorogenic and gentle COT-rhodamines for HaloTag

247

248 Self-labeling protein (SLP) tags enable chemogenetic labeling of specific cellular proteins with cell-permeable  
249 fluorophores. Compared to the fluorescent proteins (FPs), SLPs offer the mean to select between bright  
250 fluorescent probes of different colors and spectroscopic properties, making them the prime method for live-  
251 cell nanoscopy. However, the dyes attached to the tags are exposed to the cellular environment and therefore  
252 potentially phototoxic. In contrast, the chromophores of FPs are shielded to insulate the sensitization process  
253 in ROS generation<sup>48</sup>. To address the phototoxicity of SLP substrates, we coupled our gentle spirocyclic  
254 rhodamine dye to the chloroalkane HaloTag Ligand (HTL) to obtain **GR555-HTL** (19) (Fig. 4a). In addition,  
255 to broaden the spectral range and explore a different fluorophore scaffold, we synthesized the corresponding  
256 red-shifted carborhodamine derivative **GR618-HTL** (21), as an analogue to its previously published parent  
257 dye **MaP618-HTL** (20)<sup>28</sup> (Fig. 4a).

258 We compared the propensity of both probes to exist in the spirocyclic form by water-dioxane titrations:  
259 **GR555-HTL** probe is less fluorogenic ( $D_{50}$ : 40) than **MaP555-HTL** (18) ( $D_{50}$ : 66), yet it displays a mild (~4-  
260 fold) fluorescence turn-on and similar brightness when bound to HaloTag7 (Supplementary table S3 and Fig.  
261 S14a, b). **GR618-HTL** displayed a great fluorogenic potential ( $D_{50} > 75$ ) and yielded ~41-fold fluorescence  
262 turn-on upon HaloTag7 labeling (Supplementary Table S3 and Fig. S14c, d), which makes it attractive for no-  
263 wash, live-cell applications. Although *in-vitro* and live-cell labeling kinetics showed that **GR618-HTL** labeled  
264 HaloTag protein slower than **MaP618-HTL** (Supplementary Fig. S15), GR-HTL probes display equivalent  
265 signal brightness and fluorescence life-times in live-cell labeling experiments compared to their established  
266 analogues without the COT moiety (Supplementary Fig. S16, Table S3). The DPBF assay measuring singlet

267 oxygen generation demonstrated that both **GR555-HTL** and **GR618-HTL** featured lower singlet oxygen  
268 generation (by 10-/4-fold respectively) than their MaP counterparts (Supplementary Fig. S17 and Table S1).  
269

270 We then designed an *in-vitro* assay to assess the ROS damage to a functional protein that is fused to HaloTag7  
271 (Fig. 4b). Firefly luciferase (FLuc) HaloTag7-fusion protein was labeled with **GR555-HTL** or **MaP555-HTL**  
272 (Supplementary Fig. S18a-c). After green light excitation (LED 520-530 nm, 50 mW/cm<sup>2</sup>) for different periods  
273 (0 – 40 min), D-Luciferin was added and the luciferase activity was measured using a bioluminescence assay.  
274 FLuc-HaloTag7 labeled with **MaP555-HTL** exhibited a severe drop (> 85%) of enzymatic activity during the  
275 40-min illumination, indicating that the ROS generated from **MaP555-HTL** is profoundly damaging the FLuc.  
276 In contrast, FLuc-HaloTag7 labeled with **GR555-HTL** showed only a drop of < 20% after 40 min of  
277 illumination. Of note, the remaining fluorescence signal after 40 min illumination of protein samples was >  
278 60%, in which **GR555-HaloTag** was slightly more photostable than **MaP555-HaloTag** (Fig. 4c and  
279 Supplementary Fig. S18d). Therefore, we conclude that the lower phototoxicity attributed to **GR555-HTL**  
280 indeed prevents damage to closeby proteins as compared to regular **MaP555-HTL** labeling.  
281

282 To further validate the reduced phototoxicity of **GR555-HTL** at the cellular level, we fused HaloTag7 to the  
283 nuclear histone 2B (H2B). H2B is the major protein component of chromatin with a high abundance inside the  
284 nucleus. Moreover, H2B acting as the spool of DNA winding featured an extremely close spatial distance with  
285 DNA, which allowed us to assess the cellular phototoxicity of **GR555-HTL** using the XRCC1 assay (Fig. 3c).  
286 We first stained H2B-HaloTag7-expressing U-2 OS cells **GR555-HTL** or **MaP555-HTL** (500 nM each),  
287 resulting in fluorescent histone with comparable brightness (Supplementary Fig. S19). To compare the  
288 phototoxicity, we next transfected the same cells with hXRCC1-GFP and imaged its accumulation during  
289 continuous exposure to a 560 nm laser. For **MaP555-HTL**-treated samples, a uniform distribution of hXRCC1-  
290 GFP with few puncta switched to a dense scattered distribution, with a maximum puncta number of about 300-  
291 400, within 10 min of intense laser exposure. In contrast, the cells labeled with **GR555-HTL** experienced a  
292 slow increase in hXRCC1 puncta with a maximum puncta number of ~100 (Fig. 4d, e), supporting that COT  
293 conjugation significantly reduces cellular photodamage (by 3- to 4-fold) on H2B-HaloTag7 under long-term  
294 illumination. Similar results were obtained for **GR618-HTL** (Supplementary Fig. S20). Next, we targeted  
295 HaloTag7 to the outer plasma membrane by C-terminal fusion to the transmembrane domain of the platelet-  
296 derived growth factor (PDGFR<sup>tmb</sup>, pDisplay sequence) and stained mEGFP-HaloTag7-PDGFR<sup>tmb</sup> expressing  
297 HeLa cells with 500 nM **MaP555-HTL** or **GR555-HTL**, reaching a similar brightness on the plasma  
298 membrane (Fig. 4f, g). During time-lapse confocal recordings, severe rupture of plasma membrane structures  
299 was recorded in cells labeled with **MaP555-HTL** after 85 min (800 frames), as characterized by the formation  
300 of blebs. In contrast, **GR555-HTL**-labeled cells did not undergo significant apoptosis during up to 214 min  
301 (2000 frames) of time-lapse imaging (Fig. 4f, g and Supplementary Movie S2). Also, more dynamic behaviors  
302 of the plasma membrane were observed and less apoptosis arose when employing Gentle Rhodamine HaloTag7  
303 probes than traditional probes for long-term imaging (Fig. 4f and Supplementary Fig. S21).  
304

305 The red dye **GR618-HTL** opens new possibilities for spectral multiplexing and super-resolution imaging with  
306 low phototoxicity and excellent photostability. First, it can be combined with orange probes like **GR555-DNA**  
307 and near-infra-red probes like **GR650M** for multi-color imaging. We combined those probes to stain primary  
308 rat hippocampal neurons expressing CalR-HaloTag7-KDEL and recorded a 4 h (150 frames) confocal time-  
309 lapsed video (Supplementary Fig. S22 and Movie S3) with few signs of phototoxicity. Under similar conditions,  
310 the established probes **MaP555-DNA**, **MaP618-HTL**, and **SiRM** showed a loss of mitochondrial integrity  
311 (reduction of SiRM signal) after 2 h (70 frames). Second, it can be used on commercial STED systems having  
312 a 775 nm depletion laser. To highlight the capability of this approach, we combined **GR618-HTL** and **GR650M**  
313 and recorded dual-color STED images of mitochondria and the endoplasmic reticulum (CalR-HaloTag7-KDEL)

314 in live neurons (Fig. 5a). To further boost the photostability, we synergistically combined the GR strategy with  
315 exchangeable HaloTag7 ligands (xHTLs)<sup>49</sup>. **GR618** was conjugated to an xHTL linker, giving rise to the non-  
316 covalent probes **GR618-S5 (22)** (Supplementary Fig. S23a). The photobleaching behaviors of covalent  
317 (**MaP/GR618-HTL**) and the exchangeable HaloTag substrates (**MaP/GR618-S5**) were profiled using time-  
318 lapsed STED nanoscopy on U-2 OS cells expressing TOM20-HaloTag7 (Fig. 5b). Here, **GR618-S5** exhibits a  
319 slower photobleaching rate compared to **GR618-HTL**, suggesting the compatibility of **GR618** with xHTLs  
320 which gives approximately 5-fold enhancement in photostability (Fig. 5c). This finding was confirmed with a  
321 second xHTL (Hy5, Supplementary Fig. S23). Notably, the photobleaching profiles of **MaP618** and **GR618**  
322 are largely the same. This data, along with the similar photobleaching profiles of **GR555 and MaP555** (Fig.  
323 4g), suggests that the COT conjugation alone is not able to the photostability of HaloTag-labeled rhodamines.  
324

325 Finally, we showcase long-time-lapse functional imaging on primary cells by combining **GR-HTL** probes  
326 with a chemigenetic voltage indicator. Voltron consists of genetically encoded Ace2 rhodopsin fused to  
327 HaloTag7 and a fluorescent HaloTag ligand.<sup>50</sup> Compared to FRET-based indicators employing fluorescent  
328 proteins, Voltron offers a brighter signal and a larger dynamic range<sup>51</sup>. However, use of Voltron can result in  
329 phototoxicity, hampering voltage recordings (Fig. 6a). We labeled neonatal rat cardiomyocytes (NRCMs)  
330 expressing Voltron with **GR555-HTL** or **MaP555-HTL** respectively (Fig. 6b) and monitored their activity by  
331 recording the changes in fluorescence ( $\Delta F/F_0$ ) to trace their spontaneous electrical signals. However, after  $156 \pm 25$  seconds of continuous imaging at 100 Hz, the cardiomyocytes labeled with **MaP555-HTL** stopped  
332 beating and firing due to accumulated phototoxicity (Fig. 6c, d). In contrast, cardiomyocytes labeled with  
333 **GR555-HTL** provided a continuous voltage signal for up to  $573 \pm 64$  seconds under identical imaging  
334 conditions (561 nm laser illumination at  $2.16 \text{ W/cm}^2$ ) before the firing stopped (Fig. 6c, e). Therefore, gentle  
335 rhodamines combined with self-labeling protein tags offer superior tools for the physiological time-lapsed  
336 studies of primary cells.  
338

## 339 Discussion and Conclusion

340 In this work, we demonstrate that rhodamine dyes, the privileged toolkit for live cell imaging, can be rendered  
341 less phototoxic upon the conjugation of COT at the proximal 3-carboxyl group. Contrary to our expectations,  
342 the rhodamine-COT conjugates are generally less phototoxic than parental rhodamines but exhibit  
343 unpredictable behaviors in photobleaching (Fig. 1c, 4g and Supplementary Fig. S1f, S3, S5c-d, S6c-d, S13b,  
344 and S18d). These results prompt us to reconsider the intriguing relationship between phototoxicity and  
345 photostability. Unlike Cy5 chromophore whose photobleaching is mainly attributed to cycloaddition with the  
346 triplet-state-sensitized singlet oxygen<sup>52</sup>, we speculate that the main photobleaching pathways of xanthenes may  
347 not stem from the excited triplet state<sup>32</sup>. In addition, while rhodamines emitting orange to far-red synergize  
348 well with COT conjugation, the yellow emitting **GR510M** bears a decreased fluorescence quantum yield (Table  
349 S2), corroborating a recent theoretical study on the impact of COT to the singlet states of blue dyes<sup>53</sup>.  
350 Collectively, this work offers insight into the elusive photophysics of rhodamine dyes, and establishes COT-  
351 conjugation as a general strategy for alleviating phototoxicity, if not as general a method for enhancing  
352 photostability.  
353

354 With the increasing demand for spatial and temporal resolutions in live cell imaging, we argue that  
355 phototoxicity in live-cell imaging is a fundamental challenge of growing importance<sup>5,7</sup>. In this work,  
356 photodamage was thoroughly assessed through assays ranging from *in-vitro* ROS generation, proximity protein

357 damage, cell death, and morphological and physiological alterations. We have now established TSQ  
358 conjugation as a primary approach to systematically alleviate phototoxicity<sup>11,22</sup> while minimizing the non-  
359 specific binding of dyes is another viable direction in parallel<sup>54</sup>. In the future, we will further assess and  
360 optimize the tissue permeability of gentle rhodamines towards *in vivo* applications. As rhodamines are modular  
361 building blocks that can be readily combined with state-of-the-art labeling technologies, the gentle rhodamines  
362 reported here thus represent chemical solutions to phototoxicity issues in live-cell imaging. These chemical  
363 approaches would eventually synergize with mathematical, optical, and spectroscopical approaches<sup>1,55</sup> to  
364 enable time-lapse dynamic imaging, offering long-lasting fluorescence signals that transfer into multiplexed  
365 spatial and temporal information with uncompromised physiological relevance.

## 366 Acknowledgments

367 This project was supported by funds from the Beijing Municipal Science & Technology Commission (Project:  
368 Z221100003422013 to Z.C.). We thank Prof. Yulong Li for the gift of the plasmid CMV-HaloTag7-pDisplay,  
369 Prof. Wulan Deng, and Ying Bi for the U-2 OS H2B-HaloTag7 cells, Drs. Jie Su and Yuanhe Li for single  
370 crystal data analysis, Dr. Shuzhang Liu for support on voltage imaging and data analysis, A. Bergner, D. Ginkel,  
371 A. Herold (MPIMR) for providing materials and reagents. We thank the analytical instrumentation center of  
372 Peking University, the NMR facility and optical imaging facility of the National Center for Protein Sciences at  
373 Peking University, and the MS facility of MPIMR for assistance with data acquisition.

374

## 375 Data availability

376 All data reported in this paper will be shared by the corresponding author upon reasonable request.

## 377 Conflicts of interest

378 K.J. and L.W. are inventors of the patent “Cell-permeable fluorogenic fluorophores” which was filed by the  
379 Max Planck Society, for which Spirochrome AG owns a license. Z.C., T.L., Z.Y., Y.Z., P.C., and H.Z. are  
380 inventors of a patent application protecting the compounds presented in this study which was submitted by  
381 Peking University. L.R., S.P., and K.J. own shares of Spirochrome AG. Z.C. owns shares of Genvivo tech. The  
382 remaining authors declare no competing interests.

383

## 384 Author contributions

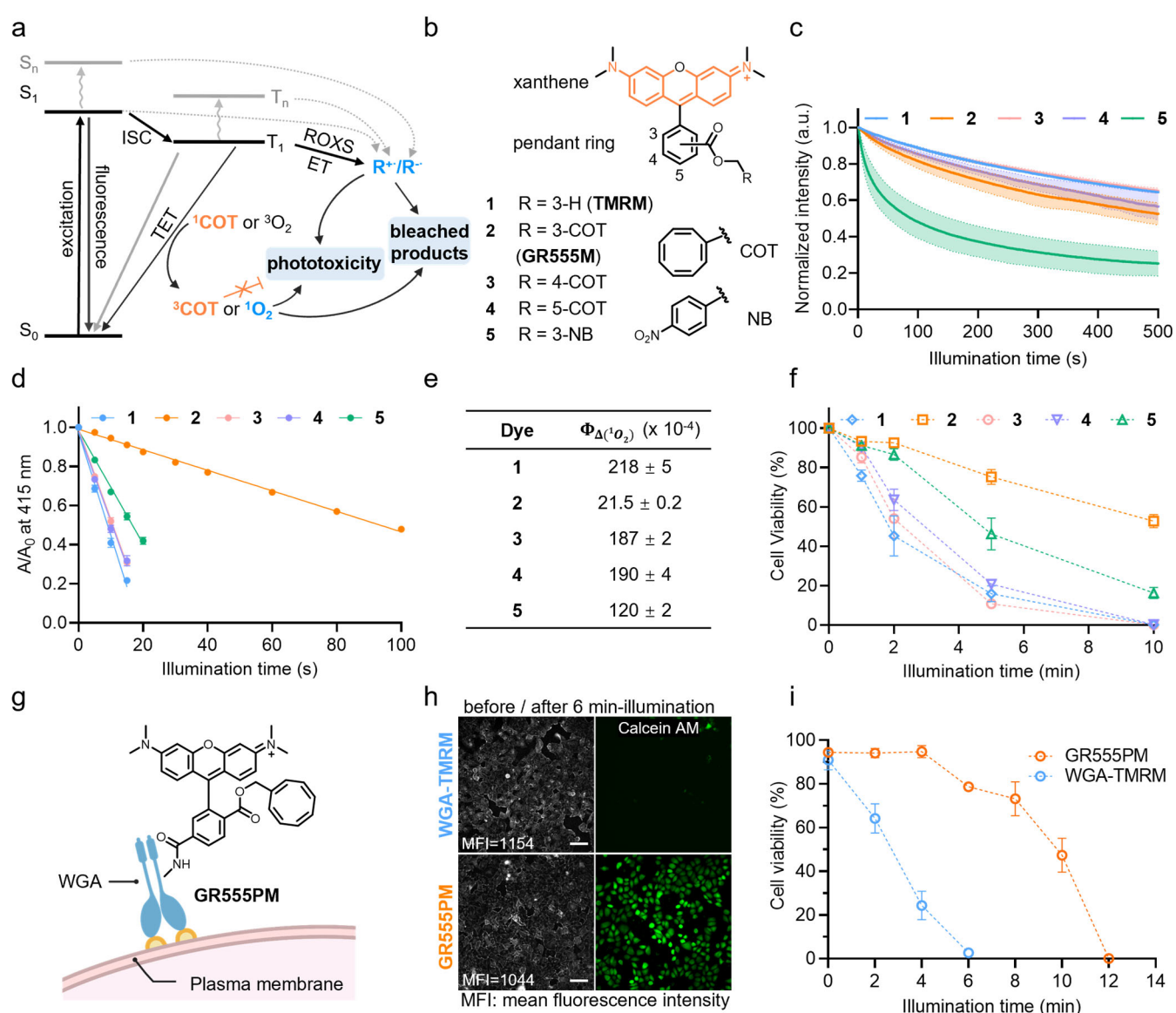
385 L.W., K. J., and Y. Z., and Z. C., independently conceived the concept and the three teams combined their  
386 efforts. T. L., J. K., and J. L. designed, performed, and analyzed the biological assays. J. C., and Z. Y.,  
387 contributed to the phototoxicity and imaging experiments. T. L., J. K., N. L., Y. Z., L. R., P. C., M. T., Z. Y.,  
388 H. Z., Y. L., and S.P. performed the chemical synthesis and characterizations. P. Z. supervised the voltage  
389 imaging assay.

390 K. J. and Z.C. supervised the project. T.L., J.K., K.J., and Z.C. wrote the paper.

391

392

393 Figures



394

395 **Figure 1. Derivatizing TMR with TSQ alleviates phototoxicity.**

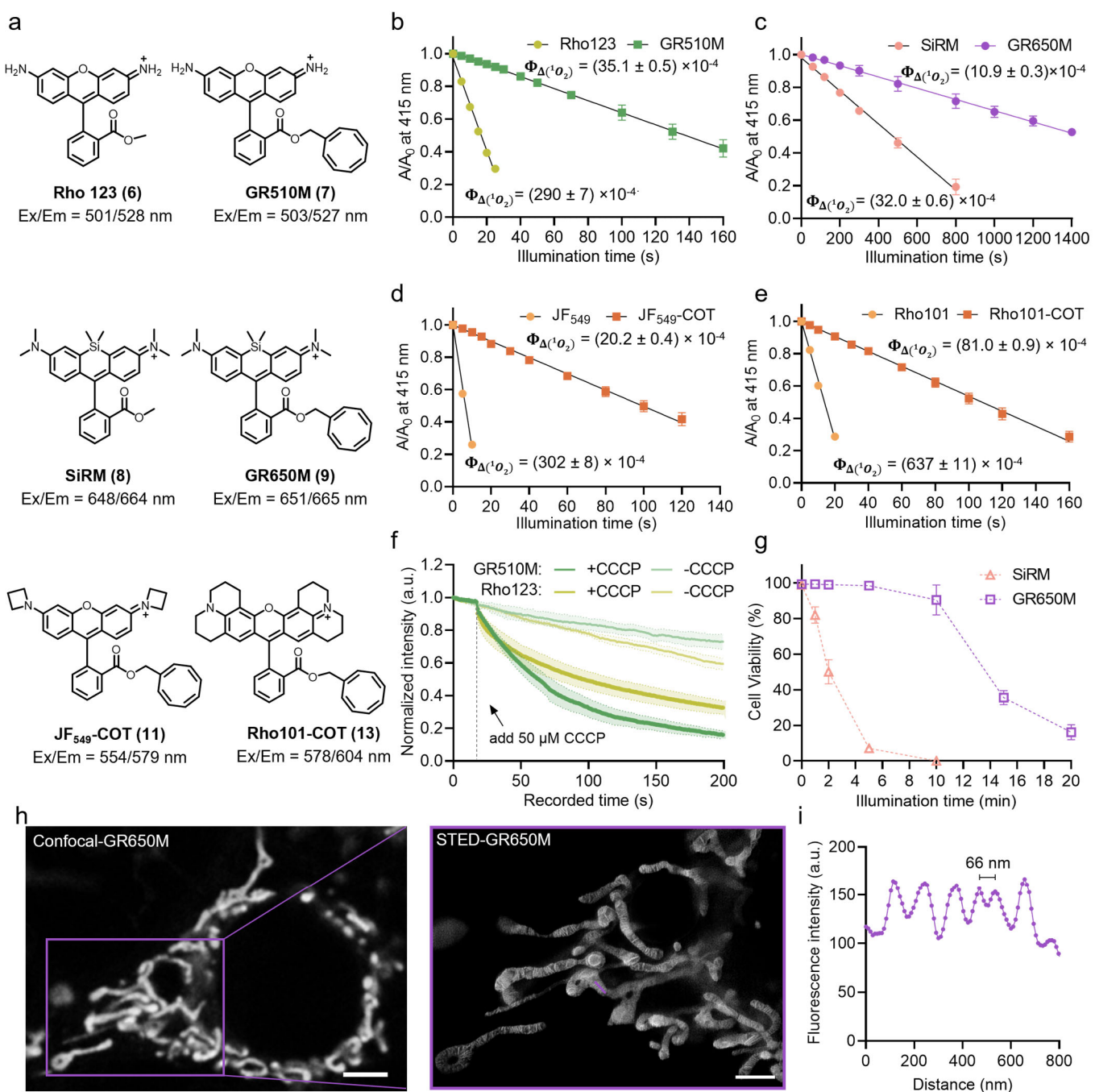
396 a. Jablonski diagram depicting different ways of relaxation from the exited state  $S_1$  including photobleaching,  
397 phototoxicity, and triplet-state quenching. ISC: Intersystem crossing; TET: Triplet-energy transfer; ROXS:  
398 reducing and oxidizing system; ET: Energy transfer.

399 b. Chemical structures of tetramethyl rhodamine-TSQs (TMR-TSQs) probes.

400 c. In-vitro photobleaching experiments of compound **1-5**. Normalized photobleaching curves of 2  $\mu$ M **1-5** embedded in  
401 hydrophobic polymethyl methacrylate (PMMA) film under a confocal microscopy. Data points represent averaged  
402 fluorescence bleaching curves of three independent replicates. Error bars, showing light-shaded areas, indicate  
403 standard deviation.

404 d. In-vitro singlet oxygen generation experiments of compound **1-5**. The maximum absorption of DPBF at 415 nm was  
405 measured under continuous irradiation with a 520-530 nm LED lamp in the presence of compound **1-5** (the absorbance  
406 of each dye at 525 nm = 0.20; concentrations: **1**, 2.2  $\mu$ M; **2**, 2.0  $\mu$ M; **3**, 2.5  $\mu$ M; **4**, 4.8  $\mu$ M; **5**, 5.8  $\mu$ M) in air-saturated  
407 acetonitrile. TMRE was used as the standard ( $\Phi_{\Delta} = 0.023$ ). Data points represent normalized and averaged DPBF  
408 bleaching curves of three independent repeats. Error bars indicate standard deviation

409 e. Absolute singlet oxygen quantum yields ( $\Phi_{\Delta}$ ) of compounds **1-5**. The decay slope of DPBF shown in **1d** is positively  
410 correlated with the singlet oxygen quantum yield. Standard deviations of three independent repeats.  
411 f. Live-cell phototoxicity measurements of compound **1-5** (250 nM, 15 min) in HeLa cells. Cell apoptosis of > 500 cells  
412 after yellow LED light illumination (561 nm, 1.4 W/cm<sup>2</sup>) was examined at each time point of the three independent  
413 experiments. Error bars indicate standard deviation.  
414 g. Schematic representation of a low-phototoxic probe, **GR555PM**, for plasma membrane labeling.  
415 h. Live-cell images of HeLa cells labeled with **WGA-TMRM** (30  $\mu$ g/ mL, 5 min) or **GR555-PM** (50  $\mu$ g/mL, 5 min)  
416 (gray) and stained with Calcein AM (1 $\mu$ M, 5 min, green) after illumination of 532 nm LED (~2.6 W/cm<sup>2</sup>) at different  
417 illumination time. Scale bars = 100  $\mu$ m.  
418 i. Live-cell phototoxicity measurements of **WGA-TMRM** and **GR555PM** in HeLa cells as shown in **1h**. Cell apoptosis  
419 of > 500 cells after green LED light illumination (532 nm, 2.6 W/cm<sup>2</sup>) were examined at each time point of the three  
420 independent experiments. Error bars indicate standard deviation.  
421



422

423 **Figure 2. Green and far-red gentle rhodamines for live-cell fluorescence microscopy of mitochondria.**

424 a. Chemical structures of compounds **6-9**, **11**, and **13** and their wavelengths of the maximum absorption and emission  
425 peaks.

426 b. In-vitro singlet oxygen generation experiments of **Rho123** (**6**) and **GR510M** (**7**). The maximum absorption of DPBF  
427 at 415 nm was measured under continuous irradiation with an 520-530 nm LED lamp in the presence of each dye  
428 (absorbance at 525 nm= 0.20; concentrations: **6**, 2.0  $\mu$ M; **7**, 2.2  $\mu$ M) in air-saturated acetonitrile. The absolute singlet  
429 oxygen quantum yields ( $\Phi_{\Delta}$ ) are given on the graph. Data points represent averaged and normalized DPBF decay  
430 curves of three independent repeats. Error bars indicate standard deviation.

431 c. In-vitro singlet oxygen generation experiments of **SiRM** (**8**) and **GR650M** (**9**). The maximum absorption of DPBF at  
432 415 nm was measured under continuous irradiation with a 620-630 nm LED lamp in the presence of each dye  
433 (absorbance at 625 nm= 0.20; concentrations: **8**, 2.5  $\mu$ M; **9**, 2.0  $\mu$ M) in air-saturated acetonitrile. The absolute singlet  
434 oxygen quantum yields ( $\Phi_{\Delta}$ ) are given on the graph. Data points represent averaged and normalized DPBF decay  
435 curves of three independent repeats. Error bars indicate standard deviation

436 d. In-vitro singlet oxygen generation experiments of **JF<sub>549</sub> (10)** and **JF<sub>549</sub>-COT (11)**. The maximum absorption of DPBF  
437 at 415 nm was measured under continuous irradiation with a 520-530 nm LED lamp in the presence of each dye  
438 (absorbance at 525 nm= 0.18; concentrations: **10**, 4  $\mu$ M; **11**, 1  $\mu$ M) in air-saturated acetonitrile. The absolute singlet  
439 oxygen quantum yields ( $\Phi_{\Delta}$ ) are given on the graph. Data points represent averaged and normalized DPBF decay  
440 curves of three independent repeats. Error bars indicate standard deviation.

441 e. In-vitro singlet oxygen generation experiments of **Rho101 (12)** and **Rho101-COT (13)**. The maximum absorption of  
442 DPBF at 415 nm was measured under continuous irradiation with a 520-530 nm LED lamp in the presence of each  
443 dye (absorbance at 525 nm = 0.1; concentrations: **12**, 2.2  $\mu$ M; **13**, 1  $\mu$ M) in air-saturated acetonitrile. The absolute singlet  
444 oxygen quantum yields ( $\Phi_{\Delta}$ ) are given on the graph. Data points represent averaged and normalized DPBF decay  
445 curves of three independent repeats. Error bars indicate standard deviation.

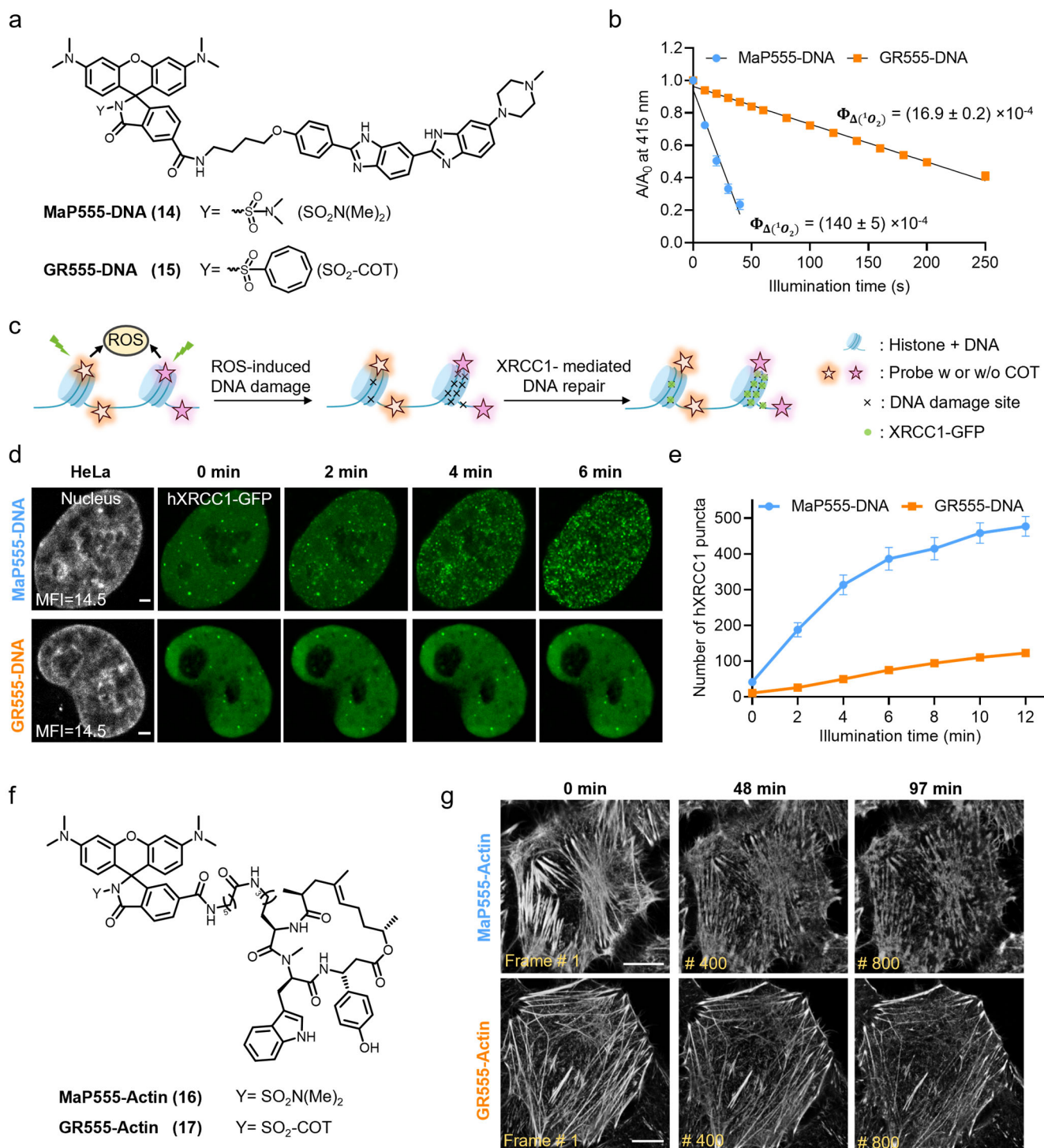
446 f. Normalized fluorescence intensities of time-lapse recordings of COS-7 cells labeled with **Rho123** or **GR510M** (300  
447 nM, 60 min) after the addition of carbonyl cyanide 3-chlorophenylhydrazone (CCCP). Control samples were treated  
448 with **Rho123** or **GR510M** without the addition of CCCP. Data points represent averaged fluorescence intensity curves  
449 of six cells from two independent biological replicates. Error bars, showing light-shaded areas, indicate standard  
450 deviation.

451 g. Phototoxicity of **GR650M** and **SiRM** (both 250 nM, 15 min) in HeLa cells, measured by cell apoptosis assay after  
452 red LED illumination (650 nm, 1.2 W/cm<sup>2</sup>) at different times. Data points indicate the mean of at least 1,500 individual  
453 cells from three independent biological repeats. Error bars indicate standard deviation.

454 h. Confocal microscopy (left) and STED nanoscopy (right, zoom in) of live COS-7 cells labeled with **GR650M** (250  
455 nM) for 15 min at 37 °C. Scale bar = 2  $\mu$ m. ( $\lambda_{\text{ex}} = 640$  nm,  $\lambda_{\text{STED}} = 775$  nm)

456 i. Fluorescence intensity line profiles measured as indicated in the magnified view of the purple boxed area in **h**.

457



459 **Figure 3. Targetable gentle rhodamines for live-cell imaging of DNA and cytoskeleton.**

460 a. Chemical structures of MaP555-DNA (14, blue) and GR555-DNA (15, orange).

461 b. In-vitro singlet oxygen generation experiments of MaP555-DNA and GR555-DNA. The maximum absorption of  
462 DPBF at 415 nm was measured under continuous irradiation with an 520-530 nm LED lamp in presence of each dye  
463 (absorbance at 525 nm = 0.15; concentrations: **14**, 1  $\mu\text{M}$ ; **15**, 1.1  $\mu\text{M}$ ) in air-saturated acetonitrile containing 0.1%TFA.  
464 The absolute singlet oxygen quantum yields ( $\Phi_{\Delta}$ ) are given on the graph. Data points represent averaged and  
465 normalized DPBF decay curves of three independent repeats. Error bars indicate standard deviation.

466 c. Schematic representation of the DNA damage assay based on hXRCC1-GFP. Upon (light-induced) DNA damage,  
467 hXRCC1-GFP gets recruited to the damaged site.

468 d. Live cell confocal images of HeLa cells expressing hXRCC1-GFP at a frame rate of 2 min/frame. HeLa cells were  
469 labeled with **MaP555-DNA** (gray, 200 nM) or **GR555-DNA** (gray, 2  $\mu\text{M}$ ) for 60 min at 37 °C. Puncta formation in

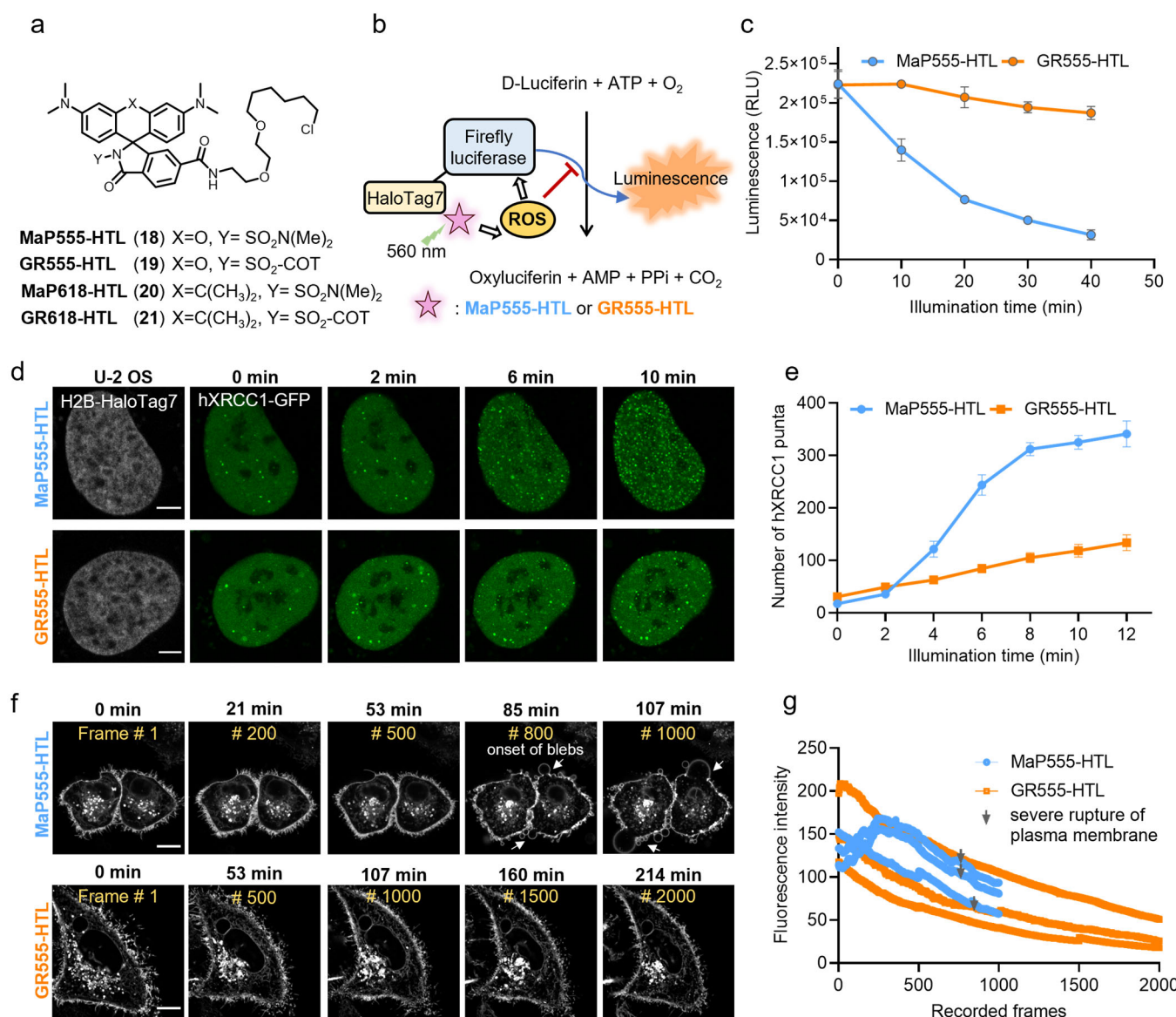
470 the time-lapse images of DNA repairing protein hXRCC1 fused with GFP indicates the DNA damage level (green).  
471 Scale bars = 2  $\mu$ m.

472 e. Semi-quantitative analysis of cellular phototoxicity of **MaP555-DNA** and **GR555-DNA** of HeLa hXRCC1-GFP cells,  
473 as measured by the total number of hXRCC1-GFP puncta from experiments shown in **d**. Data points represent the  
474 averaged hXRCC1-GFP number of eleven cells from five independent experiments. Error bars indicate the standard  
475 error of the mean.

476 f. Chemical structures of actin dyes **MaP555-Actin** (16, blue) and **GR555-Actin** (17, orange).

477 g. Long-term time-lapse confocal recordings of HeLa cells at a frame rate of 7.27 sec/frame. HeLa cells were labeled  
478 with **MaP555-Actin** or **GR555-Actin** (both 100 nM with 10  $\mu$ M verapamil) for 3 h at 37 °C. Cells labeled with  
479 **GR555-Actin** showed no shrinkage and fracture of actin filaments during the time of recording. Scale bars = 10  $\mu$ m.

480



481

482 **Figure 4. Gentle rhodamines for live-cell imaging of cellular proteins using self-labeling protein tags.**

483 a. Chemical structures of **MaP555/618**, **GR555/618** (18 – 21) derivatives coupled to the HaloTag Ligand (chloroalkane  
 484 substrate).

485 b. Schematic diagram of the protein damage assay. Firefly luciferase-HaloTag7 (FLuc-HaloTag7) is labeled with  
 486 **MaP555-618-HTL** and **GR555-618-HTL** and the photo-damage under long-term illumination assessed by the luminescence  
 487 measurements. Data points represent the averaged luminescence of three independent experiments. Error bars indicate the standard error of the mean.

488 c. Light-induced photodamage of FLuc-HaloTag7 labeled with **MaP555-618-HTL** and **GR555-618-HTL** *in-vitro*. The fully  
 489 labeled protein was illuminated and after different time points the protein damage was assessed by D-Luciferin  
 490 addition and luminescence measurements. Data points represent the averaged luminescence of three independent  
 491 experiments. Error bars indicate the standard error of the mean.

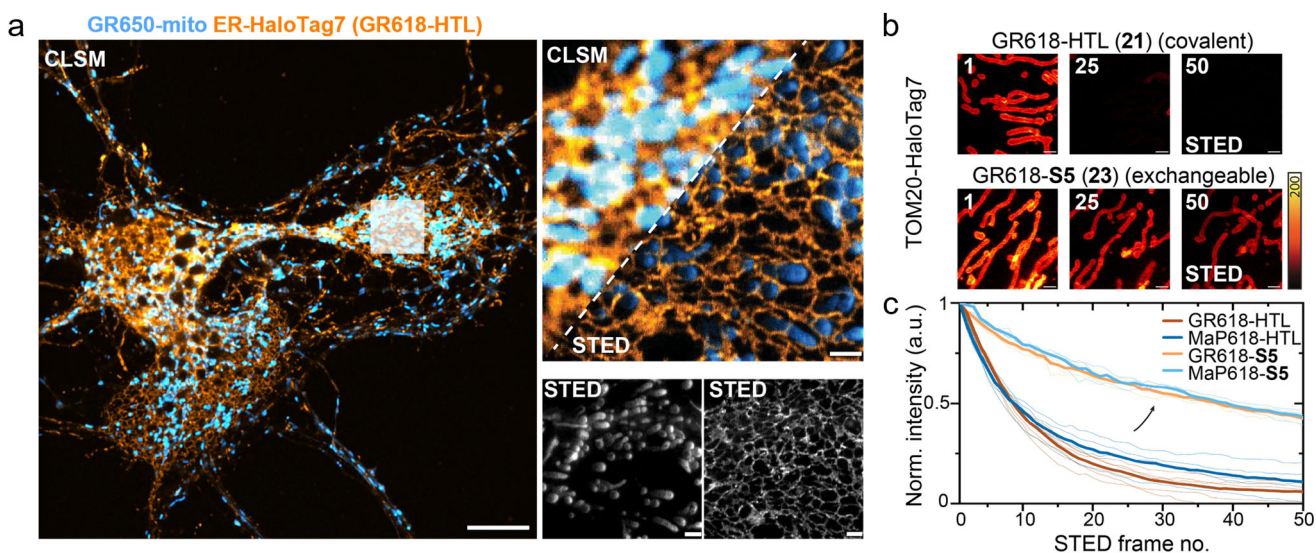
492 d. Live-cell confocal recordings (gray) of U-2 OS cells expressing H2B-HaloTag7 (stable) and DNA repairing protein  
 493 hXRCC1-GFP (transient) at a frame rate of 2 min/frame. U-2 OS cells were labeled with **MaP555-618-HTL** or **GR555-618-HTL**  
 494 (both 500 nM) for 30 min at 37 °C. Scale bars: 5 μm.

495 e. Semi-quantitative analysis of cellular phototoxicity analysis of **GR555-618-HTL** and **MaP555-618-HTL** of U-2 OS H2B-  
 496 HaloTag7 cells, as measured by counting the total number of hXRCC1-GFP puncta. Data points represent the averaged  
 497 hXRCC1-GFP number of five cells from five independent experiments. Error bars indicate the standard error of the  
 498 mean.

499 f. Long-term time-lapse confocal recordings of HeLa cells expressing HaloTag7-PDGFR<sup>tmb</sup> at a frame rate of 6.41  
500 sec/frame. HeLa cells were labeled with **MaP555-HTL** or **GR555-HTL** (both 500 nM) for 30 min at 37 °C. Cells  
501 labeled with **GR555-HTL** showed no appearance of blebs and intact plasma membrane for the time of recording.  
502 Scale bars = 10  $\mu$ m.

503 g. Photobleaching curves of HeLa cells expressing HaloTag7-PDGFR<sup>tmb</sup> labeled with **MaP555-HTL** or **GR555-HTL**  
504 under continuous time-lapse confocal recordings using a 561 nm pulsed laser. The gray arrows indicate the onset of  
505 blebbing and membrane disruption. Each curve represents the bleaching curve of an individual HeLa cell.

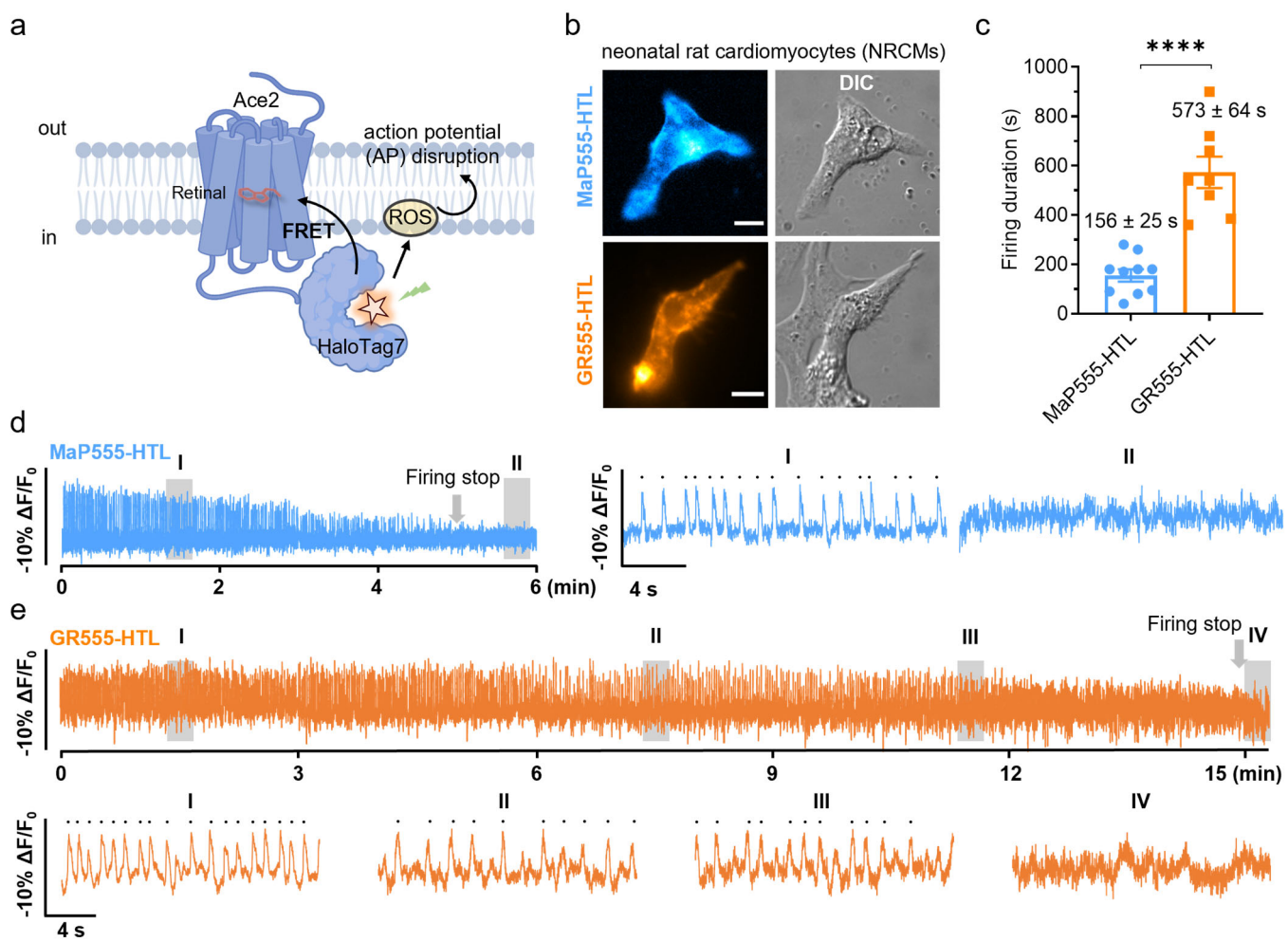
506



**a.** Dual-color confocal laser-scanning microscopy (CLSM) and STED imaging of the ER and mitochondria using gentle rhodamine probes in live cultured rat hippocampal neurons. Neurons (10 DIV) expressing CalR-HaloTag7 (rAAV transduction) were stained with **GR618-HTL** (cyan, 500 nM) and **GR650M** (red, 50 nM) for 30 min at 37 °C. **GR618-HTL** was excited with a 561 nm laser and **GR650M** with a 640 nm laser. Both dyes were depleted with a 775 nm depletion laser (STED). White rectangle in the CLSM overview (right) shows magnified FOV for STED imaging. Scale bars = 10 μm (overview), 2 μm (magnification).

**b.** Time-lapse STED imaging showcasing different photobleaching behavior of **MaP/GR618** covalently conjugated to HaloTag (HTL) or its exchangeable counterpart (S5). Multi-frame STED imaging of U-2 OS mitochondria outer membrane (TOM20-HaloTag7) labeled with **GR618-(x) HTLs** over 50 consecutive frames in a 10 × 10 μm ROI using **MaP618/GR618-HTL, -S5**. Frame numbers are indicated in the top left corner. Scale bars: 1 μm.

**c.** Bleaching curves (thick lines: mean value, thin lines: individual experiments) plotted for at least 4 image series ( $n \geq 4$ ) as shown in **b**.



522 **Figure 6. Gentle rhodamines are privileged dyes for voltage imaging of primary cells.**

523 **a.** Schematic representation of phototoxicity during long-term voltage imaging based on chemogenetic voltage-indicator  
524 **b.** Wide-field microscopy of the neonatal rat cardiomyocytes (NRCMs) expressing Voltron (Ace2-HaloTag7) and labeled  
525 with **MaP555-HTL** or **GR555-HTL** (both 100 nM) for 25 min at 37 °C. Scale bar = 10  $\mu$ m.  
526 **c.** Firing duration of NRCMs expressing Voltron (Ace2-HaloTag7) labeled with **MaP555-HTL** or **GR555-HTL**. The  
527 illumination intensities of 561 nm lasers were 2.16 W·cm<sup>-2</sup>. Bars indicate the mean of seven cells. Error bars indicate  
528 the standard error of the mean. Significance was determined using a two-tailed unpaired t-test followed by Sidak's  
529 multiple comparisons test.  $P=**** < 1.0 \times 10^{-4}$ .  
530 **d. & e.** A representative fluorescence trace of NRCMs expressing Voltron and labeled with **MaP555-HTL** or **GR555-HTL**.  
531 Each peak on the traces showed spontaneous spikes of each NRCM and signals were corrected for  
532 photobleaching. The illumination intensity of the 561 nm laser was 2.16 W/cm<sup>2</sup>.  
533 **d.** 6 min (36,000 frames) recordings at 100 frames/sec were performed. Two zoomed-in signals (i-ii) from two shaded  
534 regions (I-II) were presented at the right. Each black dot represents one spontaneous spike.  
535 **e.** 15 min (90,000 frames) recordings at 100 frames/sec were performed. Four zoomed-in signals (i-iv) from four  
536 shaded regions (I-IV) were presented at the bottom. Each black dot represents one spontaneous spike.  
537

522

523

524

525

526

527

528

529

530

531

532

533

534

535

536

537

538

539

540 Reference

541 1 Huang, X. *et al.* Fast, long-term, super-resolution imaging with Hessian structured illumination microscopy. *Nat. Biotechnol.* **36**, 451-459 (2018).

542 2 Gwosch, K. C. *et al.* MINFLUX nanoscopy delivers 3D multicolor nanometer resolution in cells. *Nat. Methods* **17**, 217-224 (2020).

543 3 Westphal, V. *et al.* Video-Rate Far-Field Optical Nanoscopy Dissects Synaptic Vesicle Movement. *Science* **320**, 246-249 (2008).

544 4 Tosheva, K. L., Yuan, Y., Matos Pereira, P., Culley, S. & Henriques, R. Between life and death: strategies to reduce phototoxicity in super-resolution microscopy. *J. Phys. D* **53**, 163001(2020).

545 5 Kilian, N. *et al.* Assessing photodamage in live-cell STED microscopy. *Nat. Methods* **15**, 755-756 (2018).

546 6 Daddysman, M. K., Tycon, M. A. & Fecko, C. J. in *Photoswitching Proteins: Methods and Protocols* (ed Sidney Cambridge) 1-17 (Springer New York, 2014).

547 7 Laissue, P. P., Alghamdi, R. A., Tomancak, P., Reynaud, E. G. & Shroff, H. Assessing phototoxicity in live fluorescence imaging. *Nat. Methods* **14**, 657-661 (2017).

548 8 Dixit, R. & Cyr, R. Cell damage and reactive oxygen species production induced by fluorescence microscopy: effect on mitosis and guidelines for non-invasive fluorescence microscopy. *Plant J.* **36**, 280-290 (2003).

549 9 Dahl, T. A., Robert Midden, W. & Hartman, P. E. Pure exogenous singlet oxygen: Nonmutagenicity in bacteria. *Mutat. Res.-Fund. Mol. M.* **201**, 127-136 (1988).

550 10 Cadenas, E. biochemistry of oxygen toxicity. *Annu. Rev. Biochem.* **58**, 79-110 (1989).

551 11 Yang, Z. *et al.* Cyclooctatetraene-conjugated cyanine mitochondrial probes minimize phototoxicity in fluorescence and nanoscopic imaging. *Chem. Sci.* **11**, 8506-8516 (2020).

552 12 Redmond, R. W. & Kochevar, I. E. Spatially resolved cellular responses to singlet oxygen. *Photochem. Photobiol.* **82**, 1178-1186 (2006).

553 13 Agostinis, P. *et al.* Photodynamic therapy of cancer: An update. *CA Cancer J. Clin.* **61**, 250-281 (2011).

554 14 Wojtovich, A. P. & Foster, T. H. Optogenetic control of ROS production. *Redox. Biol.* **2**, 368-376 (2014).

555 15 Srinivas, U. S., Tan, B. W. Q., Vellayappan, B. A. & Jeyasekharan, A. D. ROS and the DNA damage response in cancer. *Redox. Biol.* **25**, 101084 (2019).

556 16 Wäldchen, S., Lehmann, J., Klein, T., van de Linde, S. & Sauer, M. Light-induced cell damage in live-cell super-resolution microscopy. *Sci. Rep.* **5**, 15348 (2015).

557 17 Magidson, V. & Khodjakov, A. Circumventing photodamage in live-cell microscopy. *Methods Cell Biol.* **114**, 545-560 (2013).

558 18 Rajendraprasad, G., Rodriguez-Calado, S. & Barisic, M. SiR-DNA/SiR-Hoechst-induced chromosome entanglement generates severe anaphase bridges and DNA damage. *Life Science Alliance* **6**, e202302260 (2023).

559 19 Altman, R. B. *et al.* Cyanine fluorophore derivatives with enhanced photostability. *Nat. Methods* **9**, 68-71 (2012).

560 20 van der Velde, J. H. M. *et al.* A simple and versatile design concept for fluorophore derivatives with intramolecular photostabilization. *Nat. Commun.* **7**, 10144 (2016).

561 21 Grenier, V. *et al.* Molecular Prosthetics for Long-Term Functional Imaging with Fluorescent Reporters. *ACS Cent. Sci.* **8**, 118-121 (2022).

562 22 Liu, T. *et al.* Multi-color live-cell STED nanoscopy of mitochondria with a gentle inner membrane stain. *Proc. Natl. Acad. Sci. U.S.A.* **119**, e2215799119 (2022).

563 23 Liu, S. *et al.* Orange/far-red hybrid voltage indicators with reduced phototoxicity enable reliable long-term imaging in neurons and cardiomyocytes. *Proc. Natl. Acad. Sci. U.S.A.* **120**, e2306950120 (2023).

564 24 Lukinavičius, G. *et al.* A near-infrared fluorophore for live-cell super-resolution microscopy of cellular proteins. *Nat. Chem.* **5**, 132-139 (2013).

584 25 Lukinavičius, G. *et al.* Fluorogenic probes for live-cell imaging of the cytoskeleton. *Nat. Methods* **11**, 731-733 (2014).  
585 26 Lukinavičius, G. *et al.* SiR-Hoechst is a far-red DNA stain for live-cell nanoscopy. *Nat. Commun.* **6**, 8497 (2015).  
586 27 Wang, L., Frei, M. S., Salim, A. & Johnsson, K. Small-Molecule Fluorescent Probes for Live-Cell Super-Resolution  
587 Microscopy. *J. Am. Chem. Soc.* **141**, 2770-2781 (2019).  
588 28 Wang, L. *et al.* A general strategy to develop cell permeable and fluorogenic probes for multicolour nanoscopy. *Nat.*  
589 *Chem.* **12**, 165-172 (2020).  
590 29 Grimm, J. B. *et al.* A general method to improve fluorophores for live-cell and single-molecule microscopy. *Nat.*  
591 *Methods* **12**, 244-250 (2015).  
592 30 Grimm, J. B. *et al.* A general method to fine-tune fluorophores for live-cell and in vivo imaging. *Nat. Methods* **14**,  
593 987-994 (2017).  
594 31 Kolmakov, K. *et al.* A Versatile Route to Red-Emitting Carbopyronine Dyes for Optical Microscopy and Nanoscopy.  
595 *Eur. J. Org. Chem.* **2010**, 3593-3610 (2010).  
596 32 Butkevich, A. N., Bossi, M. L., Lukinavičius, G. & Hell, S. W. Triarylmethane Fluorophores Resistant to Oxidative  
597 Photobluing. *J. Am. Chem. Soc.* **141**, 981-989 (2019).  
598 33 Grimm, J. B. *et al.* A General Method to Improve Fluorophores Using Deuterated Auxochromes. *JACS Au* **1**, 690-  
599 696 (2021).  
600 34 Roßmann, K. *et al.* N-Methyl deuterated rhodamines for protein labelling in sensitive fluorescence microscopy. *Chem.*  
601 *Sci.* **13**, 8605-8617 (2022).  
602 35 Uno, S.-n. *et al.* A spontaneously blinking fluorophore based on intramolecular spirocyclization for live-cell super-  
603 resolution imaging. *Nat. Chem.* **6**, 681-689 (2014).  
604 36 Lardon, N. *et al.* Systematic Tuning of Rhodamine Spirocyclization for Super-resolution Microscopy. *J. Am. Chem.*  
605 *Soc.* **143**, 14592-14600 (2021).  
606 37 Los, G. V. *et al.* HaloTag: A Novel Protein Labeling Technology for Cell Imaging and Protein Analysis. *ACS Chem.*  
607 *Biol.* **3**, 373-382 (2008).  
608 38 Keppler, A. *et al.* A general method for the covalent labeling of fusion proteins with small molecules in vivo. *Nat.*  
609 *Biotechnol.* **21**, 86-89 (2003).  
610 39 Hein, B. *et al.* Stimulated Emission Depletion Nanoscopy of Living Cells Using SNAP-Tag Fusion Proteins. *Biophys.*  
611 *J.* **98**, 158-163 (2010).  
612 40 Mo, J. *et al.* Third-Generation Covalent TMP-Tag for Fast Labeling and Multiplexed Imaging of Cellular Proteins.  
613 *Angew. Chem. Int. Ed.* **61**, e202207905 (2022).  
614 41 Werther, P. *et al.* Bio-orthogonal Red and Far-Red Fluorogenic Probes for Wash-Free Live-Cell and Super-resolution  
615 Microscopy. *ACS Cent. Sci.* **7**, 1561-1571 (2021).  
616 42 Butkevich, A. N., Bossi, M. L., Lukinavičius, G. & Hell, S. W. Triarylmethane Fluorophores Resistant to Oxidative  
617 Photobluing. *J. Am. Chem. Soc.* **141**, 981-989 (2019).  
618 43 Zheng, Q. *et al.* Electronic tuning of self-healing fluorophores for live-cell and single-molecule imaging. *Chem. Sci.*  
619 **8**, 755-762 (2017).  
620 44 Entradas, T., Waldron, S. & Volk, M. The detection sensitivity of commonly used singlet oxygen probes in aqueous  
621 environments. *J. Photochem. Photobiol. B, Biol.* **204**, 111787 (2020).  
622 45 Monsigny, M., Roche, A.-C., Sene, C., Maget-Dana, R. & Delmotte, F. Sugar-Lectin Interactions: How Does Wheat-  
623 Germ Agglutinin Bind Sialoglycoconjugates? *Eur. J. Biochem.* **104**, 147-153 (1980).  
624 46 Caldecott, K. W. XRCC1 protein; Form and function. *DNA Repair* **81**, 102664 (2019).  
625 47 Ryumina, A. P. *et al.* Flavoprotein miniSOG as a genetically encoded photosensitizer for cancer cells. *Biochim.*  
626 *Biophys. Acta. Gen. Subj.* **1830**, 5059-5067 (2013).  
627 48 Surrey, T. *et al.* Chromophore-assisted light inactivation and self-organization of microtubules and motors. *Proc. Natl.*  
628 *Acad. Sci. U.S.A.* **95**, 4293-4298 (1998).  
629 49 Kompa, J. *et al.* Exchangeable HaloTag Ligands for Super-Resolution Fluorescence Microscopy. *J. Am. Chem. Soc.*  
630 **145**, 3075-3083 (2023).

631 50 Abdelfattah, A. S. *et al.* Bright and photostable chemigenetic indicators for extended in vivo voltage imaging. *Science*  
632 **365**, 699-704 (2019).

633 51 Vogt, N. A bright future for voltage imaging. *Nat. Methods* **16**, 1076-1076 (2019).

634 52 Gorka, A. P., Nani, R. R. & Schnermann, M. J. Cyanine polyene reactivity: scope and biomedical applications. *Org.*  
635 *Biomol. Chem.* **13**, 7584-7598 (2015).

636 53 Chanmungkalakul, S., Abedi, S. A. A., Hernández, F. J., Xu, J. & Liu, X. The dark side of cyclooctatetraene (COT):  
637 Photophysics in the singlet states of “self-healing” dyes. *Chin. Chem. Lett.*, 109227 (2023).

638 54 Zhang, J. *et al.* Red- and Far-Red-Emitting Zinc Probes with Minimal Phototoxicity for Multiplexed Recording of  
639 Orchestrated Insulin Secretion. *Angew. Chem. Int. Ed.* **60**, 25846-25855 (2021).

640 55 Ludvikova, L. *et al.* Near-infrared co-illumination of fluorescent proteins reduces photobleaching and phototoxicity.  
641 *Nature Biotechnology*, doi:10.1038/s41587-023-01893-7 (2023).

642